Correlations between turbulent wall pressure and velocity field fluctuations in backward-facing step flows

Istvan Bolgar,* Sven Scharnowski, and Christian J. Kähler

Bundeswehr University Munich, Institute of Fluid Mechanics and Aerodynamics, Werner-Heisenberg-Weg 39, 85577, Neubiberg, Germany

Abstract

The combination of high-resolution planar PIV with high frequency dynamic pressure transducers allows for the correlation of velocity field fluctuations with wall pressure fluctuations. This technique was successfully applied at the TWM facility in order to resolve the driving flow mechanisms that create the dynamic pressure loads aft of a BFS. Experiments at $Ma_\infty = 0.8$ were conducted, while PIV and pressure data were recorded simultaneously over $33\,\mathrm{s}$ at $15\,\mathrm{Hz}$ and $25\,\mathrm{kHz}$, respectively. By offsetting the pressure data, which is correlated with the PIV images by a few samples, it is possible to statistically track the dominant flow phenomenon in space and time, thus artificially increasing the temporal resolution of PIV. This allows for the determination of important fluid mechanic properties such as the convection velocity of the dominant fluid motion, as well as the vortex shedding frequency. The results show that the most dominant phenomenon exciting the dynamic loads aft of a BFS are the Kelvin-Helmholtz vortices in the reattaching shear layer, occuring at a Strouhal number normalized to the step height of $Sr_h = 0.13$.

1 Introduction

In the trans- and supersonic flow regimes it becomes increasingly difficult with increasing flow velocities to conduct temporally resolved particle image velocimetry (PIV), especially with small scale models. High-frequency pressure transducers on the other hand, offer the capability to measure with frequencies exceeding 100 kHz. However, these are only pointwise measurements and do not give information about the entire velocity field. Therefore, these two measurement techniques were combined at the Trisonic Wind Tunnel Munich (TWM), with the idea that the instantaneous velocity fields can be correlated with the signals from the pressure transducers [2]. This not only allows for the correlation of the temporally corresponding pressure signal to its vector field,

---

*e-mail: istvan.bolgar@unibw.de

but it also makes it possible to correlate a prior or future pressure signal to that vector field. This makes it possible to track coherent structures up to the temporal resolution of the pressure sensors, while retaining the high quality imaging characteristics of an sCMOS PIV camera.

Looking at the temporal behavior of a turbulent shear layer behind a BFS, the entire region of reverse flow fluctuates with several modes [14]. It has also recently been shown that the strong fluctuations are caused by large-scale periodic coherent structures with a length of several step heights that form aft of the step [9, 10]. These phenomena cause high dynamic loads on the reattachment surface aft of the step, making a planar BFS relevant for research on the aft body aerodynamics of space launchers.

The instantaneous large-scale structures have also been found to appear in very similar fashion on axisymmetric BFS models [13]. However, not only the structures are comparable between a planar and an axisymmetric model, but also the major relevant parameters such as the shear layer instability and its growth rate [4]. Therefore it can be assumed that there is a strong similarity between the driving mechanisms of a planar and an axisymmetric BFS flow. Additionally, a planar model offers the advantages that the model is not suspended into the test section via a sword mount or a sting, thus allowing to have measurements without additional aerodynamic influences.

A remaining question is which flow phenomenon is the most dominant one, causing the major pressure fluctuations on the reattachment surface. Statnikov et al. have found two major modes occuring within the flow aft of the BFS, one at a Strouhal number of $Sr_h = 0.01$ and a second one at $Sr_h = 0.07$ [14]. However, it hasn't been analyzed, whether these modes are responsible for the dominant loads on the reattachment surface. That question will be answered throughout this work.

2 Experimental set-up

2.1 The test facility

All experiments were conducted in the Trisonic Wind Tunnel (TWM) at the Bundeswehr University Munich, which is a blow-down type wind tunnel with an operating total pressure range of $1.2 - 5$ bar and a Mach number range of $0.15 - 3$. Figure 1 shows some of the key features of this measurement facility. Up to 20 bar (above ambient) of pressurized dry air is stored in two tanks (2), holding a total volume of $356 \, \mathrm{m}^3$. Typically, the air is a few Kelvin above ambient temperature at rest, after the tanks have been pressurized by up to three compressors (1). The test section (6) is $300 \, \mathrm{mm}$ wide and $675 \, \mathrm{mm}$ high with suction capabilities at both, the horizontal and the vertical walls. The side wall suction capability of the wind tunnel was taken advantage of, in order to get rid of the low momentum boundary layers on the side walls of the test section, which provides for a more homogeneous flow distribution in the spanwise direction. By setting a desired total pressure, the Reynolds number can be varied between $3.9 \times 10^6 - 8.1 \times 10^7 \, \mathrm{m}^{-1}$. The Mach number in the test section is controlled by a variable diffuser/nozzle (7) downstream of the test section up until sonic conditions. Above this, a variable Laval nozzle (5) can also be adjusted in order to reach supersonic conditions. Both, the diffuser as well as
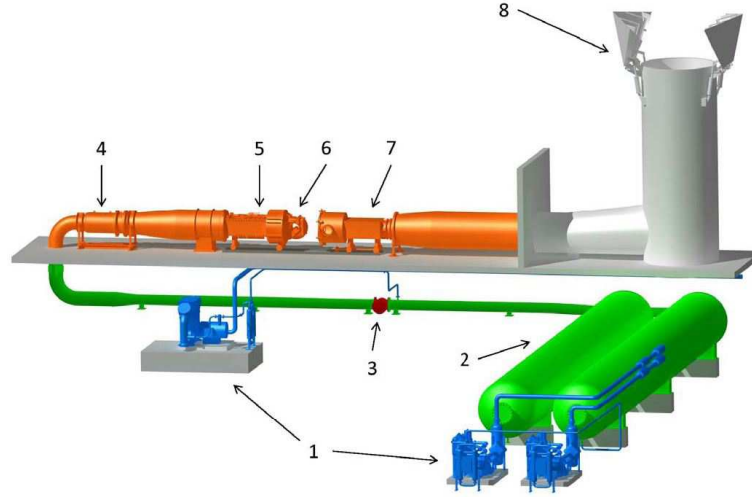
Figure 1: Trisonic Wind Tunnel Munich: (1) compressors, (2) tanks, (3) gate valve, (4) control valve, (5) variable Laval nozzle, (6) test section, (7) variable diffuser/nozzle, (8) exhaust tower

the Laval nozzle can be adjusted with infinite increments, while the Laval nozzle always takes the shape of an ideal contour nozzle, providing uniform flow above sonic conditions.

2.2   Test case & BFS model

A freestream Mach number of $Ma_\infty = 0.8$ was examined over the generic space launcher model, yielding a Reynolds number of $Re_h = 180,000$ with respect to the step height (refer to table 1 for detailed flow conditions). The quasi-2D generic space launcher model is symmetric about its horizontal plane and spans across the entire test section. It has a 150 mm long gently curved nose, in order to ensure subsonic conditions locally at a freestream Mach number of $Ma_\infty = 0.8$ [13]. The nose then transitions into a 105 mm long flat plate prior to the step. The step is 7.5 mm high on both sides and attaches to a 150 mm long splitter plate mimicking of the nozzle fairing. The overall model's thickness is 25 mm, while the step height to step width ratio is 1 : 40, providing an unaffected recirculation region due to side wall effects [3].

On one side the splitter plate was fitted with 24 dynamic pressure sensors (Kulite XCQ-062) in the center of the model, aligned in parallel to the stream-wise direction starting at $0.5h$ up to $12h$, with a constant spacing of $0.5h$. For reference purposes the model was also fitted with 24 static pressure ports in the same axial locations as the the dynamic pressure ports, however offset by 36 mm in the spanwise direction. Figure 2 provides a sketch with some details of the model.

Table 1: Freestream flow conditions of TWM for the experiment

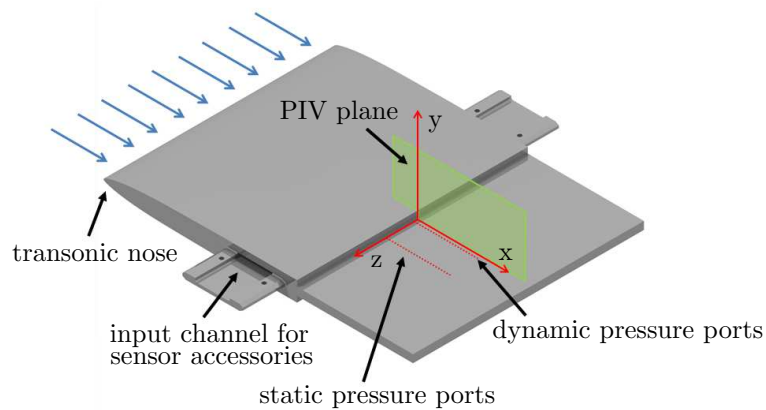| Ma_∞	U_∞ $[\frac{m}{s}]$	p_0 [bar]	p_∞ [bar]	T_0 [K]	T_∞ [K]	Re_h
0.8	259	1.73	1.129	291	258	180,000

Figure 2: Illustration of the planar space launcher model with its pressure ports and the field of view under investigation

2.3 Particle image velocimetry

For the statistical analysis of the flow field in a streamwise veritcal plane, instantaneous flow fields were computed with particle image velocimetry (PIV). For this a double pulse laser with $200\,mJ$ per pulse illuminated Di-Ethyl-Hexyl-Sebacat (DEHS) tracer particles with a mean diameter of $1\,\mu m$ [5], which are added just downstream of the control valve of the wind tunnel. The particle images were focused onto a 2560×2160 pixel sensor of an sCMOS camera with a $50\,mm$ objective. 500 double images with a statistically independent frequency of $15\,Hz$ were recorded. The time separation between an image pair was $1.6\,\mu s$, limiting the particle image shift to about $10-15$ pixel in the outer flow. This ensures that the error due to curved streamlines or the out-of-plane motion of particles is acceptably low [11, 12].

The data processing consisted of a pre-processing step, the PIV evaluation itself, and a post-processing step. The pre-processing step was comprised of an image shift correction in order to compensate for camera vibrations and subtracting the background reflections by means of proper orthogonal decomposition (POD) [7]. Instantaneous PIV images, used for statistical analyses such as the two-point correlations, had a final interrogation window size of 8×8 pixel with 50 percent overlap, yielding a vector grid spacing of $140\,\mu m$.
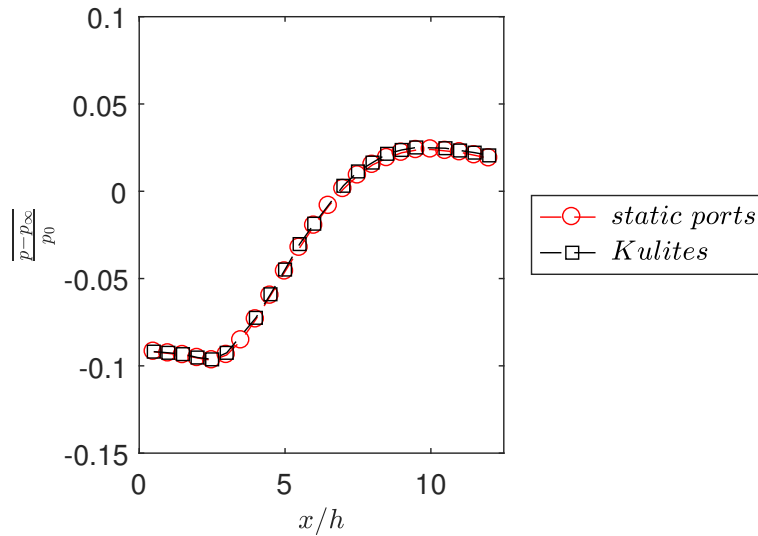
Figure 3: Comparison of the static vs. the dynamic mean pressure coefficients at $Ma_\infty = 0.8$

2.4 Dynamic pressure measurements

In addition to the PIV measurements, dynamic pressure measurements were also conducted. These measurements were carried out simultaneously to the PIV measurements. The 24 dynamic sensors were sampled simultaneously with a frequency of $25.6\,\text{kHz}$ gathering $852,000$ samples, while the static pressure ports were sampled with $200\,\text{Hz}$. At the recording frequency of the dynamic sensors, about 10 samples per period of the higher frequency mode found by Statnikov et al. are resolved at $Ma_\infty = 0.8$, which occur around $2380\,\text{Hz}$ or $Sr_h = 0.07$ [14]. Both, the static and dynamic pressure ports were given a reference pressure from the freestream at $x/h \approx -30$, hence measuring the difference to the pressure in the test section's freestream. The dynamic pressure ports were calibrated simultaneously by applying various pressures ranging from 0.2 to $1.8\,\text{bar}$ absolute onto the membranes and measuring their voltages. This resulted in a calibration curve for each sensor. After calibration, the unfiltered mean values of the dynamic senors were compared to the static values and showed a near perfect match (refer to figure 3). Note that the dynamic sensors at $x/h = 3.5, 6.5\,\&\,10$ were not measured, as some of the 24 available electrical ports were used to also measure pressure fluctuations in the freestream and ahead of the step simultaneously.

2.5 Combined PIV/pressure measurements

By measuring PIV simultaneously to the pressure at various locations, it is possible to correlate the velocity fluctuations to the pressure fluctuations. The triggering event of the PIV system and the pressure sensors was set up to work simultaneously, so that each vector field can be assigned to a certain pressure measurement. When the 500 corresponding pressure signals at $t = t_i$ are cor-

related to their 500 velocity fields, the pressure fluctuations at one pressure port have been correlated to a component of the velocity fluctuations in the 2D velocity plane, as described by Pearson's correlation coefficient in equation 1 [8].

$$R_{pu}(x,y) = \frac{\sum\limits_{i=1}^{N}[p_i(x) - \overline{p}(x)][u_i(x,y) - \overline{u}(x,y)]}{\sqrt{\sum\limits_{i=1}^{N}[p_i(x) - \overline{p}(x)]^2 \sum\limits_{i=1}^{N}[u_i(x,y) - \overline{u}(x,y)]^2}} \tag{1}$$

The idea to artificially improve the temporal resolution of PIV by means of pressure transducers involves the shifting of the pressure signals by $t\prime$, and correlating temporally offset pressure signals to the vector fields. This means that a set of pressure signals recorded prior or after the double images were taken, can show what is happening after and before in relation to the images. This allows for a statistical tracking of coherent structures over time. Each correlation image shows the correlation between the 500 velocity fields to 500 pressure measurements with an offset of $t\prime$, as can be seen in equation 2.

$$R_{pu}(x,y,t) = \frac{\sum\limits_{i=1}^{N}[p(x,t_i - t\prime) - \overline{p}(x)][u_i(x,y) - \overline{u}(x,y)]}{\sqrt{\sum\limits_{i=1}^{N}[p(x,t_i - t\prime) - \overline{p}(x)]^2 \sum\limits_{i=1}^{N}[u_i(x,y) - \overline{u}(x,y)]^2}} \tag{2}$$

3   Results

When looking at the pressure-velocity correlations, it becomes evident that the dominant flow structure causing the pressure fluctuations is in form of Kelvin-Helmholtz instabilities (refer to figure 4). This can especially be seen when correlating the y-component of the velocity fluctuations with the pressure fluctuations at $x/h = 6$, as seen in figure 4. At $t\prime = 0$ the correlation peak of R_{pu} is right above the pressure transducer at $x/h = 6$. By having correlated the temporally offset pressure signals at $t\prime = -78\,\mu s$ and at $t\prime = 78\,\mu s$ (2 time steps before and after $t\prime = 0$) to the PIV images, one can statistically track the most dominant structures in space and time.

The displacement of the negative and positive correlation peaks can be tracked over time, yielding the convection velocity of these structures at a certain streamwise location aft of the step (refer to figure 5). A convection velocity of $U_c = 148 \pm 6\,\text{m/s}$ at $x/h \approx 5.75$ was identified. The accuracy of this quantity depends on the uncertainty of the correlation peaks, thus the value is provided with an error estimation. To determine the frequency of the coherent structures, the only other variable needed is the wavelength or periodicity of the structures. This can also be determined from the correlation peaks, as the distance from one positive to the next positive correlation center (or negative to negative) portrays the wavelength. The wavelength of the structures at $x/h \approx 5.75$ is $\lambda \approx 35\,\text{mm}$. By dividing the convection velocity with the wavelength, one is left with the frequency. The most dominant frequency at $Ma_\infty = 0.8$ for instance, occurs around $f_s = 4200\,\text{Hz}$, according to the PIV/pressure correlations. This was also verified with the spectrum of the same sensor (located at $x/h = 6$), showing a
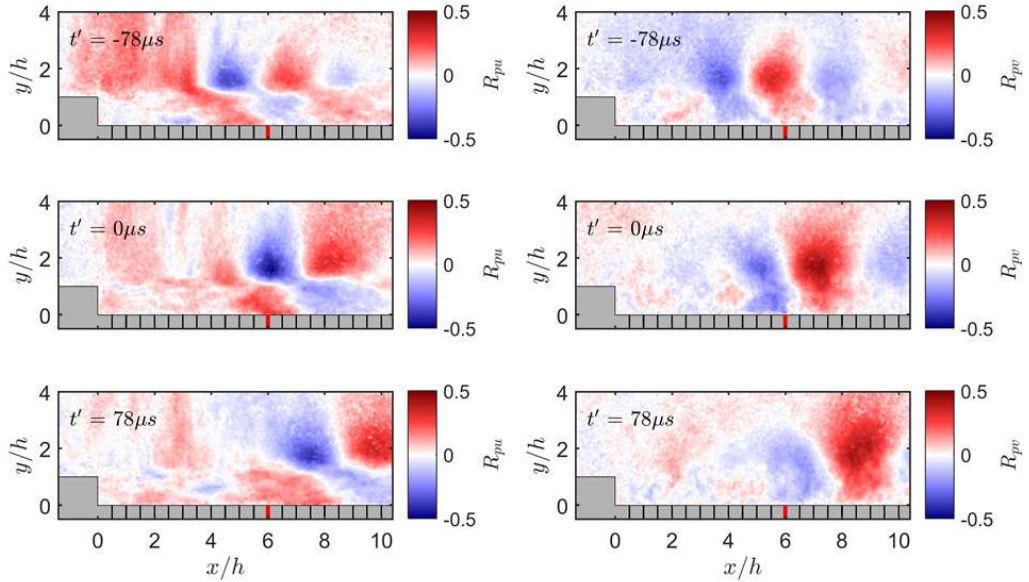
Figure 4: Velocity field fluctuations to pressure fluctuations ($x/h = 6$) at $Ma_\infty = 0.8$. Left column shows R_{pu}, right column shows $R_p v$. Images from top to bottom are offset by two time steps of the pressure transducers or $t\prime = 78\,\mu s$

broadband peak around 4400 Hz (refer to figure 6) or a $Sr_h = 0.13$. The peaks in spectrum below 2000 Hz have been verified to be the natural frequency of the TWM, while the other small peak around 2400 Hz ($Sr_h = 0.07$) corresponds to a shear layer flapping mode, as shown by Statnikov et al. [14]. This mode does not cause the alteration of the reattachment location, thus this frequency peak only shows up close to the mean reattachment location.

For the transonic regime, it can be concluded that the Kelvin-Helmholtz vortices are the driving factor for the most dominant pressure fluctuations. Even though they may be very three-dimensional in nature, statistically they occur clearly in a coherent way when displayed on a PIV plane, such as the FOV field of view (FOV) under investigation. For the future it would be interesting to investigate a streamwise horizontal FOV, to see whether the pressures correlate with finger-like structures as shown by Scharnowski et al. [10] at the same frequency. This would indicate the structures to be in the shape of horse shoe vortices.

Overall the combined PIV/pressure correlation technique showed that it is possible to extract the dominant loads on the reattaching surface while assigning them to a coherent flow phenomenon. With a Strouhal number of $Sr_h = 0.13$, the frequency of this coherent flow motion is also significantly higher than that found with large-eddy simulations carried out on the same model at the same flow conditions. There the most dominant stable frequency was determined to be at $Sr_h = 0.07$, according to Statnikov et al. [14], which is nearly lower by a factor of two.
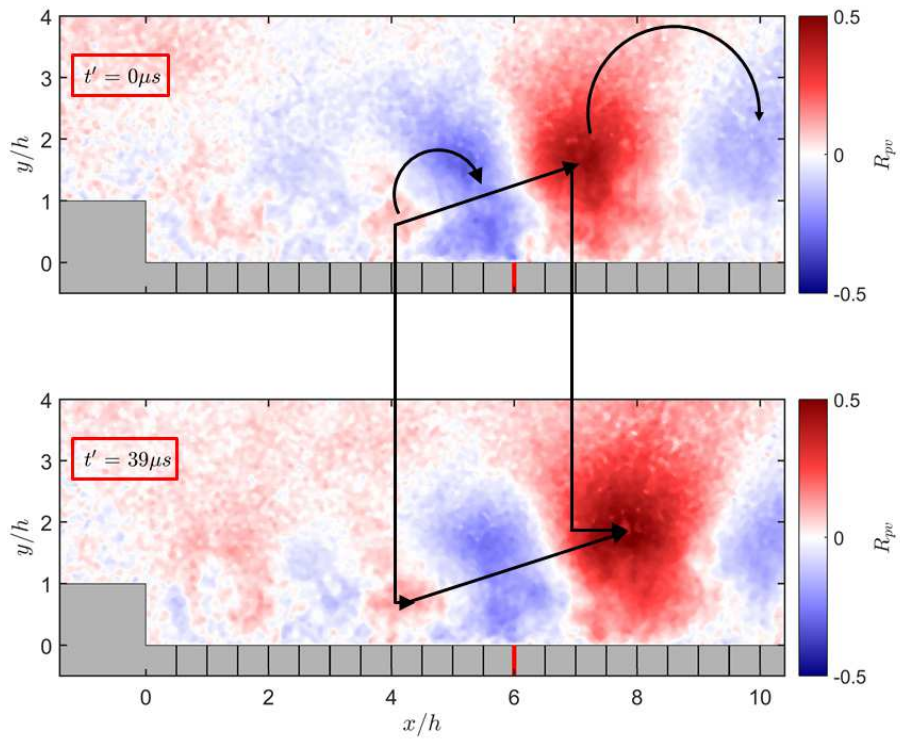
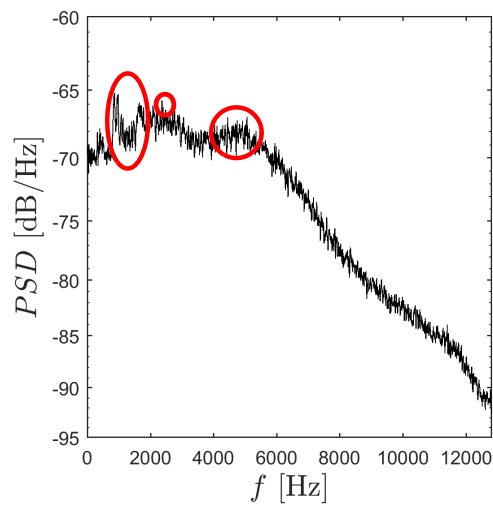Figure 5: Calculation of the convection velocity and vortex shedding frequency

Figure 6: Spectrum of the pressure fluctuations at $x/h = 6$ at $Ma_\infty = 0.8$

4   Conclusions

By using PIV and dynamic pressure transducers simultaneously, it is possible to determine the dominant flow phenomenon or mode that drives the load fluctuations experienced by the reattachment surface aft of a BFS. At $Ma_\infty = 0.8$, Kelvin-Helmholtz vortices are the driving force for the dominant pressure fluctuations. By offsetting the pressure signals correlated to the velocity fields by a few samples, it was possible to track them statistically in time to come up with the vortex shedding frequency, which for $Ma_\infty = 0.8$ is around $f_s = 4200\,\text{Hz}$ or $Sr_h = 0.13$, matching closely to the spectrum at that location as well. This is about a factor of two higher than typical dominant modes found previously in literature at comparable flow conditions.

Acknowledgments

References

[1] F. Avallone, S. Discetti, T. Astarita, and G. Cardone. Convergence enhancement of single-pixel PIV with symmetric double correlation. *Exp Fluids*, 56(4):1–11, 2015.

[2] N. A. Buchmann, Y.C. Kücükosman, K. Ehrenfried, and C.J. Kähler. Wall pressure signature in compressible turbulent boundary layers. *Progress in Wall Turbulence*, 2:93–102, 2016.

[3] V. de Brederode and P. Bradshaw. Three-Dimensional Flow in Nominally Two-Dimensional Separation Bubbles: Flow Behind a Rearward-Facing Step. Technical report, Imperial College, London, Great Britain, 1972.

[4] S. Deck and P. Thorigny. Unsteadiness of an axisymmetric separating-reattaching flow: Numerical investigation. *Phys Fluids*, 19:065103, 2007.

[5] C.J. Kähler, B. Sammler, and J. Kompenhans. Generation and control of particle size distributions for optical velocity measurement techniques in fluid mechanics. *Exp Fluids*, 33:736–742, 2002.

[6] C.J. Kähler, S. Scharnowski, and C. Cierpka. On the resolution limit of digital particle image velocimetry. *Exp Fluids*, 52:1629–1639, 2012.

[7] M.A. Mendez, M. Raiola, A. Masullo, S. Discetti, A. Ianiro, R. Theunissen, and J.-M. Buchlin. POD-based background removal for particle image velocimetry. *Exp Therm Fluid Sci*, 80:181–192, 2017.

[8] J.L. Rodgers and W.A. Nicewander. Thirteen Ways to Look at the Correlation Coefficient. *Am Stat*, 42(1):59–66, 1988.

[9] S. Scharnowski, I. Bolgar, and C.J. Kähler. Control of the recirculation region of a transonic backward-facing step flow using circular lobes. In *9th Int. Symp. on Turbulence and Shear Flow Phenomena (TSFP-9)*, Melbourne, Australia, 2015.

[10] S. Scharnowski, I. Bolgar, and C.J. Kähler. Characterization of turbulent structures in a transonic backward-facing step flow. *Flow Turbul Combust*, 2016.

[11] S. Scharnowski and C.J. Kähler. On the effect of curved streamlines on the accuracy of PIV vector fields. *Exp Fluids*, 54:1435, 2013.

[12] S. Scharnowski and C.J. Kähler. Estimation and optimization of loss-of-pair uncertainties based on PIV correlation functions. *Exp Fluids*, 57:23, 2016.

[13] V. Statnikov, Roidl B., Meinke M., and W. Schröder. Analysis of spatio-temporal wake modes of space launchers at transonic flow. In *54th AIAA Aerospace Sciences Meeting*, 2016.

[14] V. Statnikov, I. Bolgar, S. Scharnowski, M. Meinke, C.J. Kähler, and W. Schröder. Analysis of characteristic wake flow modes on a generic transonic backward-facing step configuration. *Eur J of Mech B/Fluids*, 59:124–134, 2016.